

## PAPER

[View Article Online](#)  
[View Journal](#)

## Interfacial hydrogen-bond modulation of dynamic catalysts for nitrate electroreduction to ammonia†

Cite this: DOI: 10.1039/d5ee00597c

Yuchi Wan,<sup>a</sup> Yixiang Tang,<sup>a</sup> Yinze Zuo,<sup>\*a</sup> Kaian Sun,<sup>a</sup> Zewen Zhuang,<sup>a</sup> Yun Zheng,<sup>a</sup> Wei Yan,<sup>a</sup> Jiujun Zhang<sup>\*a</sup> and Ruitao Lv<sup>id</sup> <sup>\*b</sup>

Electrocatalytic nitrate reduction ( $\text{NO}_3^-$ RR) holds significant potential for clean  $\text{NH}_3$  synthesis and the treatment of industrial effluents, effectively converting waste into a valuable resource. However, the catalyst reconstruction mechanism remains ambiguous, and the influence of interfacial hydrogen bonds on  $\text{NO}_3^-$ RR performance remains underexplored. Herein, a Cr-doping strategy was developed to regulate the interfacial hydrogen-bonded interactions on Co-based dynamic electrocatalysts to improve electrocatalytic  $\text{NO}_3^-$ RR activity. *In situ* XRD, *in situ* Raman spectroscopy and theoretical calculations indicated that Cr doping could modulate the reconstruction process of Co-based materials, achieving a dynamic balance between  $\text{Co}(\text{OH})_2$  and Co. Moreover, molecular dynamics simulations and density functional theory calculations, combined with *in situ* infrared spectroscopy, revealed that the strong hydrogen-bonding interactions between interfacial  $\text{H}_2\text{O}$  and the Cr-doped  $\text{Co}(\text{OH})_2$  surface could drag more free  $\text{H}_2\text{O}$  from the rigid  $\text{H}_2\text{O}$  network and facilitate  $\text{H}_2\text{O}$  dissociation, forming active hydrogen to accelerate the  $\text{NO}_3^-$ RR pathway on metallic Co sites. As a result, the Cr-doped Co-based dynamic electrocatalyst displayed a superior  $\text{NH}_3$  faradaic efficiency of 97.36% and a high  $\text{NH}_3$  yield rate of  $58.92 \text{ mg h}^{-1} \text{ cm}^{-2}$ , outperforming the state-of-the-art electrocatalysts. This work can further inspire the design of dynamic electrocatalysts and the modulation of the interfacial microenvironment for promoting effective electrochemical hydrogenation reactions.

Received 31st January 2025,  
Accepted 10th April 2025

DOI: 10.1039/d5ee00597c

rsc.li/ees

## Broader context

Ammonia ( $\text{NH}_3$ ), an indispensable feedstock for fertilizer supply, chemical production, and a source of hydrogen, is mainly produced by the Haber–Bosch process, which is associated with high energy consumption and significant  $\text{CO}_2$  emissions. Electrocatalytic nitrate reduction ( $\text{NO}_3^-$ RR) offers the potential to utilize green electrical energy for simultaneous clean  $\text{NH}_3$  synthesis and industrial effluent disposal, turning waste into a valuable resource. However, the development of efficient electrochemical ammonia synthesis faces two primary challenges: dynamic catalyst design and modulation of the interfacial microenvironment. In this work, a Cr-doping strategy is proposed to modulate the interfacial hydrogen bond in Co-based dynamic electrocatalysts, enhancing the electrocatalytic nitrate reduction to ammonia. As a result, the Cr-doped Co-based dynamic electrocatalyst displays a superior  $\text{NH}_3$  faradaic efficiency of 97.36% and a high  $\text{NH}_3$  yield rate of  $58.92 \text{ mg h}^{-1} \text{ cm}^{-2}$ , outperforming state-of-the-art electrocatalysts. This work can further inspire dynamic electrocatalyst design and interfacial microenvironment modulation for electrochemical hydrogenation reactions.

## Introduction

Ammonia ( $\text{NH}_3$ ), an essential feedstock for fertilizer production, chemical manufacturing and hydrogen generation, is

mainly synthesized through the Haber–Bosch process under harsh conditions, resulting in significant energy consumption and  $\text{CO}_2$  emissions.<sup>1</sup> Consequently, there is an urgent need to develop sustainable methods for producing clean ammonia under mild conditions. Recently, electrocatalysis has emerged as a promising strategy for green ammonia synthesis by harnessing electricity from renewable energy sources.<sup>2</sup> However, the high  $\text{N}\equiv\text{N}$  bond energy and the low water solubility of inert  $\text{N}_2$  significantly decrease the  $\text{NH}_3$  yield and the reaction selectivity in  $\text{N}_2$  reduction, making it challenging to meet industrial requirements.<sup>3</sup> In contrast to  $\text{N}_2$ , nitrate ( $\text{NO}_3^-$ ) has a much lower bond energy ( $204 \text{ kJ mol}^{-1}$ ) and is commonly found in wastewater from industrial discharges.<sup>4</sup>

<sup>a</sup> Institute of New Energy Materials and Engineering, Fujian Engineering Research Center of High Energy Batteries and New Energy Equipment & Systems, School of Materials Science and Engineering, Fuzhou University, Fuzhou, 350108, China. E-mail: yinzezuo@fzu.edu.cn, jiujun.zhang@fzu.edu.cn

<sup>b</sup> State Key Laboratory of New Ceramics and Fine Processing, School of Materials Science and Engineering, Tsinghua University, Beijing, 100084, China. E-mail: lvrutao@tsinghua.edu.cn

† Electronic supplementary information (ESI) available. See DOI: <https://doi.org/10.1039/d5ee00597c>

Therefore, electrocatalytic nitrate reduction ( $\text{NO}_3^-$ RR) can not only promote the yield of green  $\text{NH}_3$  but also effectively treat industrial effluents, achieving the conversion of waste into value. Nevertheless, electrocatalytic  $\text{NO}_3^-$ RR is impeded by complex reaction intermediates and sluggish reaction kinetics, resulting in limited reaction rates and selectivity.<sup>5</sup> Furthermore, other constituents in nitrate-containing wastewater may contribute to catalyst poisoning, reducing the stability of the  $\text{NO}_3^-$ RR system. The sustainable supply of nitrate presents a huge challenge to advancing the industrialization of  $\text{NO}_3^-$ RR. Additionally, the reaction rate of  $\text{NO}_3^-$ RR can be lowered by decreased nitrate concentration and limited mass transfer.<sup>6</sup> To accelerate the development of electrocatalytic  $\text{NO}_3^-$ RR, designing high-performance electrocatalysts is crucial for enhancing  $\text{NH}_3$  yield and reaction efficiency.

Co-based electrocatalysts have been considered promising candidates for electrochemical  $\text{NH}_3$  synthesis from  $\text{NO}_3^-$ RR, due to their appropriate  $\text{NO}_3^-$  adsorption ability and efficient  $\text{NO}_2^-$  removal capability.<sup>7–9</sup> It is widely recognized that Co-based materials, particularly metallic Co, tend to undergo a reconstruction process during electrocatalytic  $\text{NO}_3^-$ RR, or even in the absence of applied potentials.<sup>10–12</sup> For example, Zhang *et al.* reported a three-step pathway involving the reconstruction process of Co-based materials and the conversion of  $\text{NO}_3^-$  into  $\text{NH}_3$ .<sup>13</sup> Under open-circuit potential conditions, metallic Co could be spontaneously reduced by  $\text{NO}_3^-$ , leading to the formation of  $\text{Co(OH)}_2$  and  $\text{NO}_2^-$ . Upon applying potential,  $\text{Co(OH)}_2$  would be reduced back to Co, and  $\text{NO}_2^-$  would undergo the electrocatalytic process to produce  $\text{NH}_3$ . Their *in situ* characterizations could only detect Co in the absence of  $\text{Co(OH)}_2$  signals below 0 V vs. reversible hydrogen electrode (RHE), revealing the reduction of  $\text{Co(OH)}_2$  to Co under negative potentials. However, in the study of Pan *et al.*,  $\text{Co(OH)}_2$  was found to stably exist over a wide range of negative potentials during the electrocatalytic  $\text{NO}_3^-$ RR process.<sup>14</sup> Despite the progress in the development of Co-based catalysts, the conversion mechanism of the reconstruction process remains controversial. Additionally, the significant structural changes during reconstruction could lead to the loss of active sites or even the stripping of active materials from the electrode, thereby compromising electrocatalytic stability. Therefore, it is crucial to rationally modulate the reconstruction process of Co-based materials and elucidate the mechanisms of phase change.

As identified, electrocatalytic  $\text{NO}_3^-$ RR involves 8 electrons and 9 protons to complete the  $\text{NH}_3$  synthesis pathway, with the hydrogenation steps requiring a continuous supply of active hydrogen ( $^*\text{H}$ ).<sup>15</sup> In neutral or alkaline environments,  $^*\text{H}$  is derived from  $\text{H}_2\text{O}$  dissociation. The  $\text{H}_2\text{O}$  adsorption and dissociation processes are closely related to the interactions between interfacial  $\text{H}_2\text{O}$  and the catalyst surface.<sup>16</sup> Moreover, the more rigid the hydrogen bond network connecting the  $\text{H}_2\text{O}$  molecules, the more difficult the  $\text{H}_2\text{O}$  adsorption and dissociation processes become,<sup>17</sup> which could pose a threat to the  $^*\text{H}$  supply for the hydrogenation steps in electrochemical  $\text{NO}_3^-$ RR. However, the majority of previous research has focused on investigations of  $^*\text{H}$ , often neglecting the influence of the

interfacial  $\text{H}_2\text{O}$  structure and hydrogen-bonded interactions on electrocatalytic  $\text{NO}_3^-$ RR performance.<sup>18–20</sup> Therefore, it is crucial to effectively modulate the interfacial hydrogen bond network and disrupt the connectivity of the  $\text{H}_2\text{O}$  network to accelerate the hydrogenation conversions in  $\text{NO}_3^-$ RR.

In this work, a Cr doping strategy was employed to modulate the interfacial  $\text{H}_2\text{O}$  structure on the Co-based dynamic electrocatalyst to enhance electrocatalytic  $\text{NO}_3^-$ RR performance. The Cr-doped Co-based materials were successfully synthesized using an ion exchange method followed by a subsequent calcination process. *In situ* characterizations and theoretical calculations revealed that  $\text{CoO}_x$  could be reconstructed to  $\text{Co(OH)}_2$  and Co during the  $\text{NO}_3^-$ RR process, and Cr doping facilitated a dynamic balance between  $\text{Co(OH)}_2$  and Co. *In situ* electrochemical infrared spectra demonstrated that the Cr doping strategy effectively regulated the interfacial  $\text{H}_2\text{O}$  structure, allowing more free  $\text{H}_2\text{O}$  to participate in the hydrogenation process of  $\text{NO}_3^-$ RR. Both molecular dynamics simulations and density functional theory calculations further revealed that strong interactions between interfacial  $\text{H}_2\text{O}$  and Cr- $\text{Co(OH)}_2$  surface disrupted the rigid hydrogen bond network and promoted the  $\text{H}_2\text{O}$  dissociation, thereby accelerating the electrocatalytic  $\text{NO}_3^-$ RR process on the metallic Co site. Benefiting from the efficient regulation of the interfacial hydrogen bond network, the Cr-doped dynamic electrocatalysts exhibited high  $\text{NO}_3^-$ RR performance across a wide potential range, with a high  $\text{NH}_3$  faradaic efficiency of 97.36% and a superior  $\text{NH}_3$  yield rate of  $58.92 \text{ mg h}^{-1} \text{ cm}^{-2}$ .

## Results and discussion

### Theoretical investigations

Molecular dynamics (MD) simulations were first performed to analyse the atomic structures of interfacial  $\text{H}_2\text{O}$  on different material surfaces. The representative MD snapshots showed that the interfacial  $\text{H}_2\text{O}$  molecules could strongly interact with the Cr-doped  $\text{Co(OH)}_2$  [Cr- $\text{Co(OH)}_2$ ] surface through hydrogen bonding between the O atom of the interfacial  $\text{H}_2\text{O}$  and H atom of the  $-\text{OH}$  group from Cr- $\text{Co(OH)}_2$  (Fig. 1a). The interactions between the interfacial  $\text{H}_2\text{O}$  and the  $\text{Co(OH)}_2$  without Cr doping were much weaker, as shown in Fig. 1b. In comparison, the interfacial  $\text{H}_2\text{O}$  molecules stayed much farther away from the metallic Co surface (Fig. 1c) than from the Cr- $\text{Co(OH)}_2$  surface. Moreover, the interfacial  $\text{H}_2\text{O}$  distribution was reflected by the concentration distribution profiles of O atoms along the surface normal direction (Fig. 1d). Compared with Co and  $\text{Co(OH)}_2$ ,  $\text{H}_2\text{O}$  molecules were much closer to the Cr- $\text{Co(OH)}_2$  surface, with an increased interfacial  $\text{H}_2\text{O}$  concentration. To explore the regulatory effect of Cr doping on interfacial hydrogen bonds, the hydrogen-bond distributions along the surface normal directions of Co,  $\text{Co(OH)}_2$  and Cr- $\text{Co(OH)}_2$  were calculated, as shown in Fig. 1e. In the region  $\sim 3 \text{ \AA}$  away from the material surface (red shading), the hydrogen bonds were obviously increased for Cr- $\text{Co(OH)}_2$  due to the formation of hydrogen bonds between the interfacial  $\text{H}_2\text{O}$  and the  $-\text{OH}$

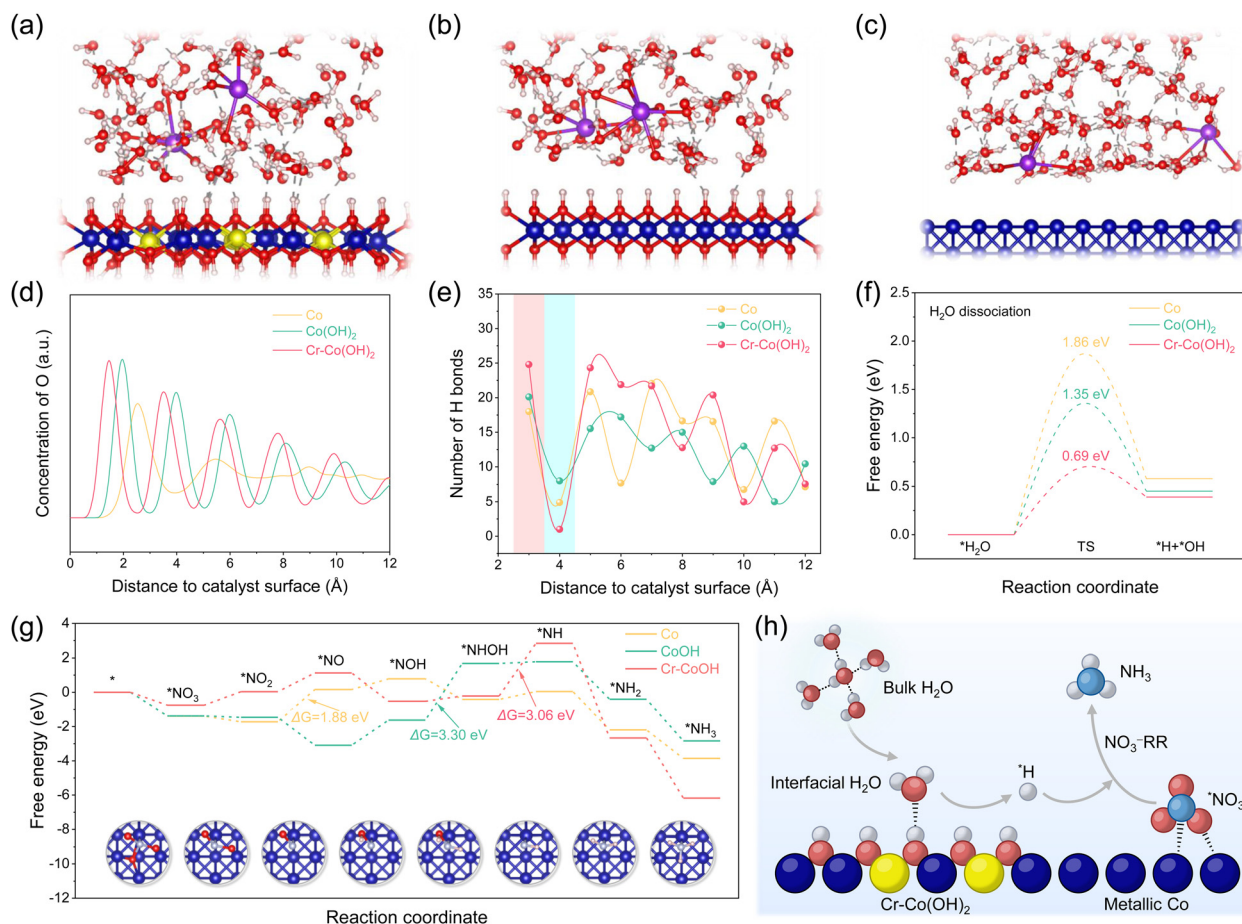


**Fig. 1** Interfacial hydrogen-bond network structure and  $\text{NO}_3^-$ -RR mechanism. Representative snapshots of the interfacial  $\text{H}_2\text{O}$  structures for (a)  $\text{Cr-Co(OH)}_2$ , (b)  $\text{Co(OH)}_2$ , and (c)  $\text{Co}$ . The Cr, Co, O, H, and K atoms are colored in yellow, blue, red, pink, and purple, respectively. The gray dashed lines represent the H bonds. (d) Concentration distribution profiles of O atoms in water along the surface normal direction of  $\text{Cr-Co(OH)}_2$ ,  $\text{Co(OH)}_2$ , and  $\text{Co}$ . (e) Statistical distribution of the number of H bonds along the surface normal directions of  $\text{Cr-Co(OH)}_2$ ,  $\text{Co(OH)}_2$ , and  $\text{Co}$ . (f) Comparison of the  $\text{H}_2\text{O}$  dissociation kinetic barriers. (g) Free energy diagrams of  $\text{NO}_3^-$ -RR on  $\text{Co}$ ,  $\text{Co(OH)}_2$ , and  $\text{Cr-Co(OH)}_2$ . The insets correspond to the adsorption structures of each intermediate on  $\text{Co}$ . (h) Schematic of the  $\text{NO}_3^-$ -RR on the  $\text{Cr-Co(OH)}_2/\text{Co}$  heterostructure with  $^*\text{H}$  participation from interfacial  $\text{H}_2\text{O}$  dissociation. The Cr, Co, O, H, and N atoms are colored in yellow, dark blue, red, grey, and light blue, respectively.

groups from  $\text{Cr-Co(OH)}_2$ . However, the number of hydrogen bonds at a distance of  $\sim 4$  Å (blue shading) was dramatically reduced for the  $\text{Cr-Co(OH)}_2$  surface, corresponding to a disruption of the hydrogen-bond networks of the interfacial  $\text{H}_2\text{O}$ .<sup>21</sup> Therefore, the above MD simulation results demonstrated that doping Cr into  $\text{Co(OH)}_2$  could strengthen the molecular interactions with interfacial  $\text{H}_2\text{O}$  and disrupt the rigid hydrogen-bond networks, thereby allowing more  $\text{H}_2\text{O}$  molecules to participate in the hydrogenation reactions.

Density functional theory (DFT) calculations were further conducted to explore the  $\text{H}_2\text{O}$  dissociation process and the  $\text{NO}_3^-$ -RR reaction pathway. The  $\text{H}_2\text{O}$  adsorption energy of  $\text{Cr-Co(OH)}_2$  was  $-1.80$  eV, which was much lower than that of  $\text{Co}$  and  $\text{Co(OH)}_2$  (Fig. S1, ESI†), indicating that interfacial  $\text{H}_2\text{O}$  molecules would thermodynamically prefer to adsorb on the  $\text{Cr-Co(OH)}_2$  surface. Moreover, the  $\text{H}_2\text{O}$  dissociation processes on different electrocatalysts were also explored. As shown in Fig. 1f,  $\text{Cr-Co(OH)}_2$  showed the lowest kinetic energy barrier for  $\text{H}_2\text{O}$  dissociation (0.69 eV) compared with  $\text{Co}$  and  $\text{Co(OH)}_2$  (Fig.

S2, ESI†), revealing that  $\text{H}_2\text{O}$  molecules were kinetically easier to dissociate with the formation of active hydrogen ( $^*\text{H}$ ) on the  $\text{Cr-Co(OH)}_2$  surface. Under the influence of hydrogen-bonding interactions,  $\text{Cr-Co(OH)}_2$  showed a low energy barrier for  $^*\text{H}$  formation from the dissociation of adsorbed  $\text{H}_2\text{O}$  in the solvated environment (Fig. S3, ESI†). Benefitting from the adequate  $^*\text{H}$  supply, the hydrogenation process of the  $\text{NO}_3^-$ -RR could thus be promoted. Besides, Cr doping could also play a significant role in suppressing the competing hydrogen evolution reaction (HER) process (Fig. S4, ESI†). Furthermore, the Gibbs free energy of each step during the  $\text{NO}_3^-$ -RR was calculated, as shown in Fig. 1g. For  $\text{Cr-Co(OH)}_2$ , the rate-determining step (RDS) was the conversion of  $^*\text{NHOH}$  into  $^*\text{NH}$  with a high energy barrier of 3.06 eV (Fig. S5, ESI†). Meanwhile, the Gibbs free energy of the RDS was 3.30 eV for  $\text{Co(OH)}_2$  (Fig. S6, ESI†). The RDS of the  $\text{NO}_3^-$ -RR on metallic  $\text{Co}$  could be turned into the deoxygenation process of  $^*\text{NO}_2$  with a much reduced energy barrier, indicating that the electrocatalytic  $\text{NO}_3^-$ -RR tended to proceed on the metallic  $\text{Co}$  sites.



Therefore,  $\text{Cr-Co(OH)}_2$  and metallic Co can serve as the active sites for  $\text{H}_2\text{O}$  dissociation and nitrate reduction to ammonia, respectively. Based on the MD simulations and DFT calculations, the synergistic catalytic mechanism of  $\text{Cr-Co(OH)}_2$  and metallic Co could be proposed, as shown in Fig. 1h. In this mechanism, Cr-doped  $\text{Co(OH)}_2$  modulated the interfacial  $\text{H}_2\text{O}$  structure and disturbed the connectivity of the hydrogen-bond network to boost  $\text{H}_2\text{O}$  adsorption and dissociation. Meanwhile, metallic Co effectively adsorbed  $\text{NO}_3^-$  and utilized the  $^*\text{H}$  derived from  $\text{H}_2\text{O}$  dissociation to accelerate the conversion of  $\text{NO}_3^-$  into the  $\text{NH}_3$  product.

### Synthesis and characterization of the materials

As a proof of concept, the Cr-doped Co-based materials were prepared by the ion exchange of ZIF-67 and a subsequent calcination process, as shown in Fig. 2a. During the ion-exchange process, the ligands of ZIF-67 were partially substituted by  $\text{CrO}_4^{2-}$  with good dispersion of Cr sites in the ZIF-67 precursor. Compared with the pristine ZIF-67, the Cr-doped

ZIF-67 after the ion exchange maintained a morphology of nanosheet arrays but with a reduced nanosheet thickness and a rougher surface (Fig. S7, ESI<sup>†</sup>), which could be ascribed to the surface etching of the precursor by  $\text{CrO}_4^{2-}$ . After proceeding with calcination in a mixed  $\text{Ar}/\text{H}_2$  atmosphere, the Cr-doped ZIF-67 was converted into Cr-doped  $\text{CoO}_x$  ( $\text{Cr-CoO}_x$ ) nanoparticles dispersed on the N-doped carbon matrix (Fig. 2b and c). The high-resolution transmission electron microscopy (HRTEM) and the corresponding fast Fourier transform (FFT) and inverse FFT (IFFT) images confirmed the existence of Co and CoO components in the  $\text{Cr-CoO}_x$  electrocatalyst (Fig. 2d and e). Moreover, the (111) plane of CoO was slightly expanded, which could be ascribed to the Cr doping. The high-angle annular dark-field scanning TEM (HAADF-STEM) and the corresponding energy dispersive spectroscopy (EDS) elemental mapping images revealed the uniform distribution of the different elements (Fig. S8, ESI<sup>†</sup>). Inductively coupled plasma optical emission spectrometry (ICP-OES) analysis indicated a Cr mass content of 6.38 wt% for the  $\text{Cr-CoO}_x$  electrocatalyst,

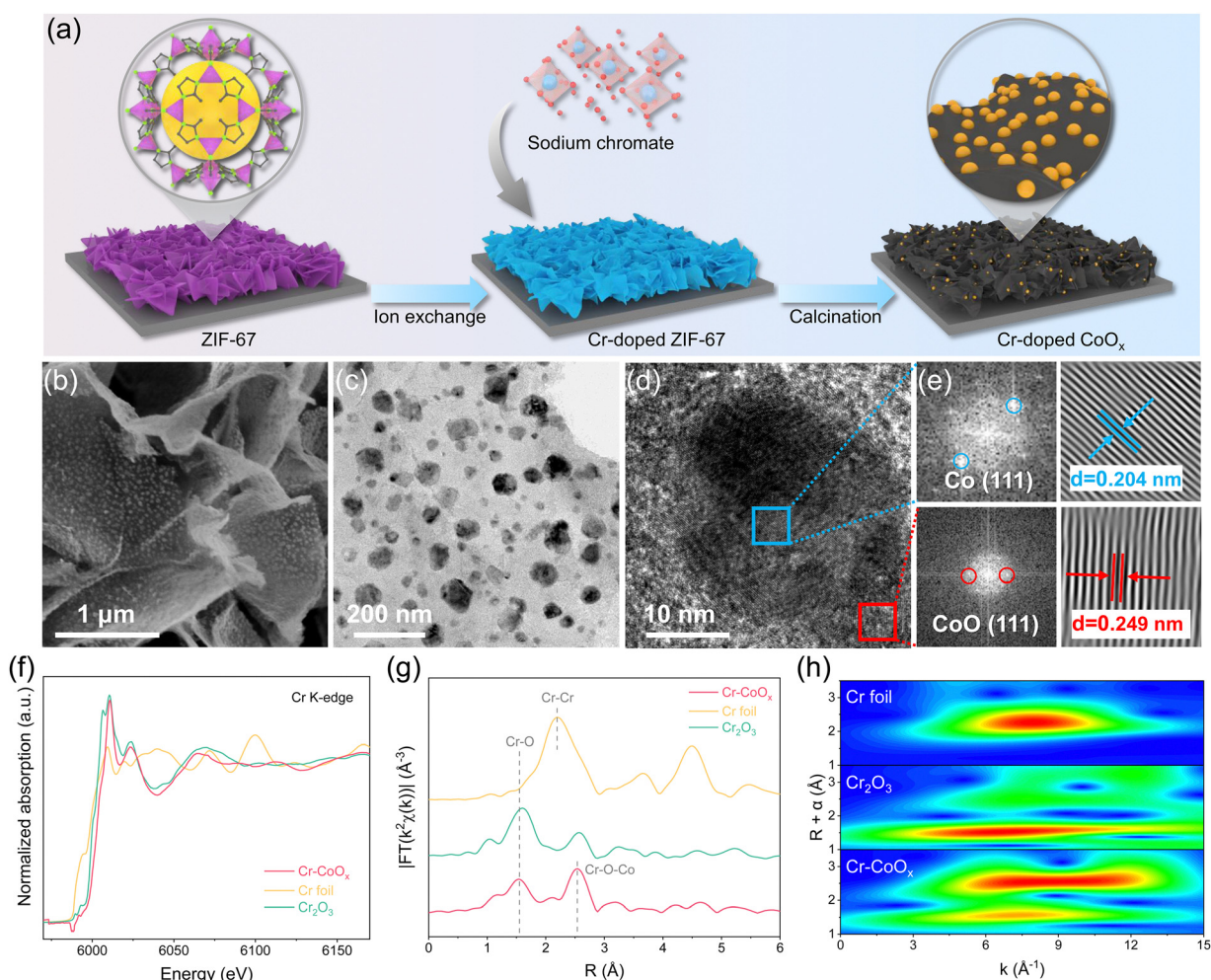


**Fig. 2** Synthesis and characterizations of the  $\text{Cr-CoO}_x$  electrocatalyst. (a) Schematic of the preparation process of the  $\text{Cr-CoO}_x$  electrocatalyst. (b) SEM, (c) TEM, (d) HRTEM, and (e) corresponding FFT and IFFT images of  $\text{Cr-CoO}_x$ . (f) Cr K-edge XANES spectra, (g) EXAFS spectra, and (h) wavelet transforms for the Cr K-edge EXAFS of  $\text{Cr-CoO}_x$  and reference samples.

which was close to the EDS elemental analysis results (Fig. S9, ESI†). To prove the universality of the material-designing strategy, the same group elements of Mo and W were also successfully introduced into the Co-based materials by a similar preparation method (Fig. S10–S12, ESI†). The X-ray diffraction (XRD) patterns of the various electrocatalysts showed similar diffraction peaks, corresponding to the Co phase (PDF# 15-0806) and CoO phase (PDF# 43-1004) (Fig. S13, ESI†), which were consistent with the TEM results.

Next, X-ray photoelectron spectroscopy (XPS) measurements were performed to explore the regulation effects of the dopants on the electronic structure of Co. As shown in the Co 2p XPS fine scan spectra (Fig. S14, ESI†), doping Cr, Mo, and W elements resulted in a positive shift of binding energy of the Co element. The Cr 2p, Mo 3d, and W 4f characteristic peaks could be identified, from the XPS fine scan spectra of the different samples (Fig. S15 and S16, ESI†). The coordination structure of the Cr-CoO<sub>x</sub> electrocatalyst was further characterized by

X-ray absorption spectroscopy. As shown in Fig. 2f, the Cr K-edge X-ray absorption near-edge structure (XANES) of Cr-CoO<sub>x</sub> was close to that of the Cr<sub>2</sub>O<sub>3</sub> reference sample, indicating that the valence state of the Cr dopant in Cr-CoO<sub>x</sub> was +3, which was consistent with the XPS result. In the Fourier transform extended X-ray absorption fine structure (EXAFS) spectrum of Cr-CoO<sub>x</sub>, two peaks were observed at 1.55 and 2.54 Å (Fig. 2g), which could be assigned to the Cr–O path from the first coordination shell and the Cr–O–Co path from the second coordination shell.<sup>22</sup> The coordination environment of the Cr dopant was further confirmed by the wavelet transforms of the EXAFS of the materials (Fig. 2h). Moreover, the Co K-edge XANES spectrum of Cr-CoO<sub>x</sub> was located between that of the Co foil and CoO reference sample (Fig. S17a, ESI†), revealing that the valence state of Co in Cr-CoO<sub>x</sub> was between 0 and +2. The Co K-edge EXAFS spectrum of Cr-CoO<sub>x</sub> displayed two peaks at 1.65 and 2.16 Å (Fig. S17b, ESI†), which corresponded to the Co–O path and Co–Co path,

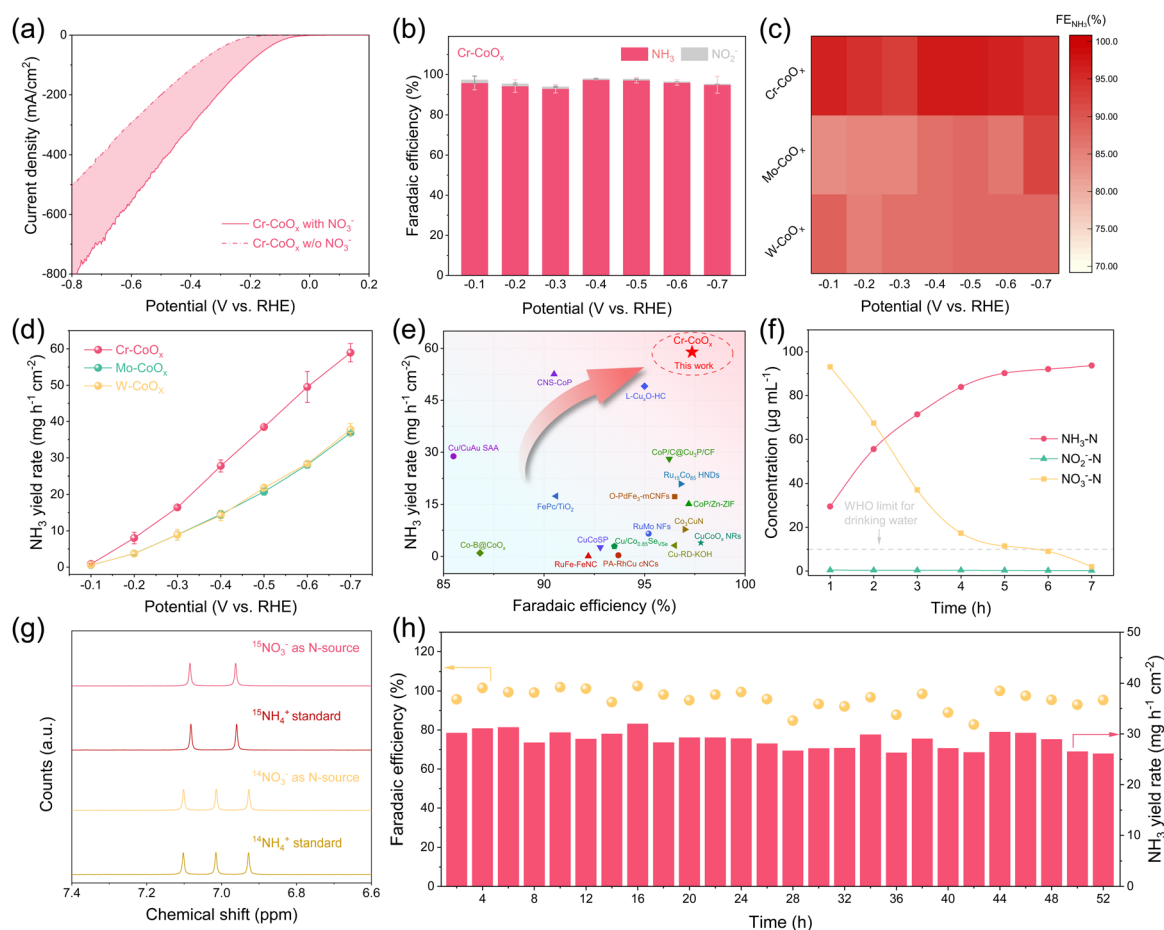


**Fig. 3** Electrocatalytic NO<sub>3</sub><sup>-</sup>RR performance evaluations. (a) LSV curves without iR compensation for the Cr-CoO<sub>x</sub> electrocatalyst in 1 M KOH with and without 0.1 M NO<sub>3</sub><sup>-</sup>. The filled area corresponds to the current density difference. (b) Faradaic efficiency of NH<sub>3</sub> and NO<sub>2</sub><sup>-</sup> for the Cr-CoO<sub>x</sub> electrocatalyst at different potentials. (c) NH<sub>3</sub> Faradaic efficiency and (d) NH<sub>3</sub> yield rate normalized to the geometric electrode area of the Cr-CoO<sub>x</sub>, Mo-CoO<sub>x</sub>, and W-CoO<sub>x</sub> electrocatalysts. (e) Comparison of NH<sub>3</sub> yield rate and Faradaic efficiency of the Cr-CoO<sub>x</sub> with other recently reported electrocatalysts. (f) Time-dependent N concentration of NH<sub>3</sub>, NO<sub>2</sub><sup>-</sup>, and NO<sub>3</sub><sup>-</sup> over the Cr-CoO<sub>x</sub> electrocatalyst at 100 mA cm<sup>-2</sup> in simulated wastewater containing 0.01 M NO<sub>3</sub><sup>-</sup>. (g) <sup>1</sup>H NMR spectra of the standard samples and the products obtained from electrocatalytic NO<sub>3</sub><sup>-</sup>RR over the Cr-CoO<sub>x</sub> electrocatalyst at -0.4 V vs. RHE using <sup>14</sup>NO<sub>3</sub><sup>-</sup> and <sup>15</sup>NO<sub>3</sub><sup>-</sup> as the feeding N sources. (h) Cycling performance of the Cr-CoO<sub>x</sub> electrocatalyst at -0.4 V vs. RHE.

respectively,<sup>23</sup> further proving the co-existence of the Co and CoO components.

### Electrocatalytic $\text{NO}_3^-$ RR performance evaluation

For the preliminary evaluation of electrocatalytic  $\text{NO}_3^-$ RR performance, linear sweep voltammetry (LSV) measurements were carried out for different electrocatalysts in 1 M KOH with or without 0.1 M  $\text{NO}_3^-$ . Obviously, the Cr-CoO<sub>x</sub> electrocatalyst showed an increased current density and a positively shifted onset potential in the presence of  $\text{NO}_3^-$  compared to the absence of  $\text{NO}_3^-$  (Fig. 3a), revealing the superior catalytic  $\text{NO}_3^-$ RR activity of the Cr-CoO<sub>x</sub> electrocatalyst in the measured potential range. Moreover, similar phenomena were also observed for the Mo-CoO<sub>x</sub> and W-CoO<sub>x</sub> electrocatalysts (Fig. S18, ESI†). Additionally, the LSV curves were further corrected with 50% iR compensation (Fig. S19, ESI†). In comparison with the Mo-doped and W-doped electrocatalysts, the Cr-CoO<sub>x</sub> electrocatalyst displayed a reduced Tafel slope in  $\text{NO}_3^-$  (Fig. S20, ESI†), indicating accelerated  $\text{NO}_3^-$ RR kinetics induced by the Cr dopant. Furthermore, potentiostatic measurements were performed in 1 M KOH containing 0.1 M  $\text{NO}_3^-$  at different potentials ranging from −0.1 V to −0.7 V vs. RHE for 1 h (Fig. S21, ESI†). The N-containing species in the electrolyte after the potentiostatic measurements were quantitatively detected *via* a colorimetric method (Fig. S22–S25, ESI†). As shown in Fig. 3b, the Cr-CoO<sub>x</sub> electrocatalyst exhibited a high faradaic efficiency for  $\text{NH}_3$  (>90%) over a wide potential range from −0.1 V to −0.7 V vs. RHE. It is worth noting that the Cr-CoO<sub>x</sub> electrocatalyst showed an optimal  $\text{NH}_3$  faradaic efficiency of 97.36% at −0.4 V vs. RHE. Compared to the CoO<sub>x</sub> electrocatalyst without Cr doping (Fig. S26, ESI†), the Cr-CoO<sub>x</sub> electrocatalyst displayed a negligible presence of the byproduct  $\text{NO}_2^-$ , particularly at low overpotentials, indicating the significant role of the Cr dopant in facilitating the hydrogenation of  $\text{NO}_2^-$ . In addition, the Cr-CoO<sub>x</sub> electrocatalyst showed a high  $\text{NH}_3$  yield rate of 58.92 mg h<sup>−1</sup> cm<sup>−2</sup> and an industrial-scale  $\text{NH}_3$  partial current density of 765.42 mA cm<sup>−2</sup> at −0.7 V vs. RHE, outperforming the CoO<sub>x</sub> electrocatalyst (Fig. S27–S28, ESI†). To explore the doping effect on  $\text{NO}_3^-$ RR performance, the electrocatalytic activities of the Mo-CoO<sub>x</sub> and W-CoO<sub>x</sub> counterparts were also tested (Fig. S29 and S30, ESI†). As a result, the Cr-doping strategy showed a remarkable advantage in promoting electrocatalytic  $\text{NO}_3^-$ RR performance compared to the Mo- or W-doping methods (Fig. 3c and d). Additionally, the Cr-CoO<sub>x</sub> electrocatalyst also displayed an increased electrochemically active surface area (ECSA) and reduced charge-transfer resistance (Fig. S31 and S32, ESI†). Overall, the Cr-CoO<sub>x</sub> electrocatalyst exhibited superior comprehensive performance for electrochemical  $\text{NH}_3$  synthesis, surpassing most state-of-the-art electrocatalysts (Fig. 3e and Table S1, ESI†).

Due to the large discrepancy in  $\text{NO}_3^-$  concentrations in real wastewater, the  $\text{NO}_3^-$ RR performances of the electrocatalysts were further evaluated in different  $\text{NO}_3^-$  concentrations. With increasing  $\text{NO}_3^-$  concentration, the current density and  $\text{NH}_3$  yield rate of the Cr-CoO<sub>x</sub> electrocatalyst were enhanced (Fig. S33, ESI†). The high faradaic efficiency for  $\text{NH}_3$  (>95%) over a

wide range of  $\text{NO}_3^-$  concentrations (0.05–0.5 M) reflected the great potential of the Cr-CoO<sub>x</sub> electrocatalyst for the treatment of  $\text{NO}_3^-$ -containing industrial effluents. After continuous  $\text{NO}_3^-$ RR measurement on the Cr-CoO<sub>x</sub> electrocatalyst for 7 h, the  $\text{NO}_3^-$  removal efficiency reached 98.6%, and the residual  $\text{NO}_3^-$  concentration was below the World Health Organization (WHO) limit for drinking water (Fig. 3f). To clarify the origin of the detected  $\text{NH}_3$ , control experiments and <sup>15</sup>N isotopic labelling experiments were conducted. The control experiments showed negligible  $\text{NH}_3$  production in the absence of  $\text{NO}_3^-$  (Fig. S34, ESI†). Next, when feeding <sup>15</sup> $\text{NO}_3^-$  or <sup>14</sup> $\text{NO}_3^-$  in the nitrate reduction process, the <sup>1</sup>H nuclear magnetic resonance (NMR) spectra showed the typical doublet peaks of <sup>15</sup> $\text{NH}_4^+$  or triplet peaks of <sup>14</sup> $\text{NH}_4^+$ , respectively (Fig. 3g), indicating that the detected ammonia originated from the electrochemical  $\text{NO}_3^-$ RR. Moreover, the  $\text{NH}_3$  yield rate was quantified by <sup>1</sup>H NMR, which were comparable to the measurement results obtained using the indophenol blue method (Fig. S35 and S36, ESI†). To evaluate the stability of the Cr-CoO<sub>x</sub> electrocatalyst, long-term cycling measurements were performed without changing the electrode. As shown in Fig. 3h, the  $\text{NH}_3$  yield rate and faradaic efficiency remained relatively stable during the cycling tests for over 50 h, confirming the excellent stability of the  $\text{NO}_3^-$ RR performance of the Cr-CoO<sub>x</sub> electrocatalyst.

### Dynamic reconstruction investigations

Considering the possible reconstruction of Co-based materials during the  $\text{NO}_3^-$ RR process, the electrocatalysts after cycling tests were further characterized in detail. It was observed that the Cr-CoO<sub>x</sub> electrocatalyst could essentially retain its pristine morphology, but with the emergence of numerous thin nanosheets on the surface (Fig. S37, ESI†). However, the Mo-CoO<sub>x</sub> and W-CoO<sub>x</sub> electrocatalysts experienced more significant reconstruction, with the formation of agglomerated nanoplates. The original structure of the CoO<sub>x</sub> electrocatalyst without doping treatment was found to have completely collapsed after the cycling tests, resulting in the residual large-size nanoplates with random distributions. The results indicated that Cr doping could modulate the reconstruction degree of Co-based electrocatalysts, preventing irreversible structural evolution. Moreover, the selected area electron diffraction (SAED) pattern and IFFT images confirmed the co-existence of Co and Co(OH)<sub>2</sub> for the Cr-CoO<sub>x</sub> electrocatalyst after the cycling tests (Fig. S38, ESI†), while the XPS spectra identified that the Cr dopant could be retained (Fig. S39, ESI†). Therefore, it could be concluded that the Cr-doped CoO<sub>x</sub> was reconstructed with the formation of the Cr-doped Co(OH)<sub>2</sub>/Co heterostructure.

In order to achieve the real-time monitoring of the reconstruction process, electrochemical *in situ* XRD and *in situ* Raman spectra measurements were carried out. As shown in the *in situ* XRD patterns of the Cr-doped electrocatalyst (Fig. 4a), the peak intensity of Co(OH)<sub>2</sub> gradually increased while the peak intensity of Co gradually decreased with a negative shift of the potentials. The mixed Co(OH)<sub>2</sub> and Co phases reached a dynamic balance when the applied potential reached −0.4 V vs. RHE. However, for the Mo-doped and W-doped electrocatalysts, the dynamic balance of Co(OH)<sub>2</sub>/Co could be disrupted, with a



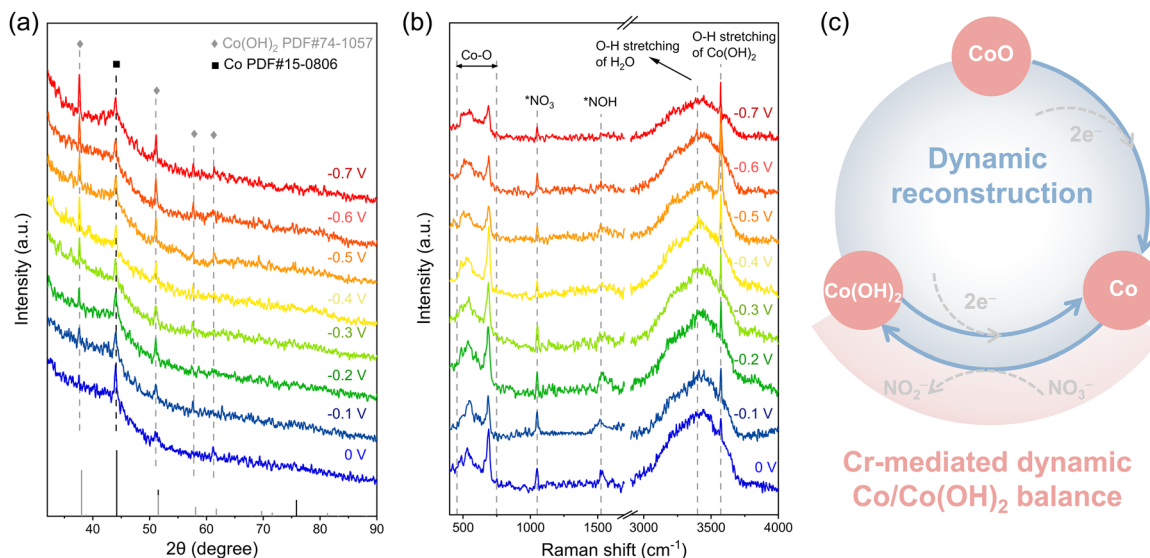
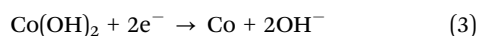
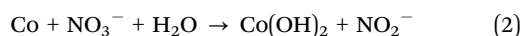
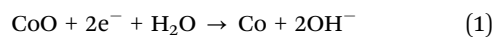


Fig. 4 *In situ* characterizations of the dynamic reconstruction process. (a) *In situ* electrochemical XRD patterns and (b) *in situ* electrochemical Raman spectra of the Cr-CoO<sub>x</sub> electrocatalyst. (c) Schematic of the Cr-mediated dynamic reconstruction mechanism.

much stronger diffraction peak of Co(OH)<sub>2</sub> than that of Co (Fig. S40 and S41, ESI†). The CoO<sub>x</sub> electrocatalyst without doping treatment showed both weak peaks for Co(OH)<sub>2</sub> and Co in the *in situ* XRD patterns (Fig. S42, ESI†), indicating that the crystalline phase structure had been severely damaged during the electrocatalytic NO<sub>3</sub><sup>−</sup>RR process. Furthermore, *in situ* Raman spectroscopy measurements were also conducted to demonstrate the formation of Co(OH)<sub>2</sub> during the reconstruction process. As shown in Fig. 4b, the characteristic peaks at 485, 542, and 689 cm<sup>−1</sup> could be ascribed to the Co–O bond vibration modes of Co(OH)<sub>2</sub>,<sup>24</sup> while the peak at 3571 cm<sup>−1</sup> corresponded to the –OH stretching vibration of Co(OH)<sub>2</sub>.<sup>25</sup> Based on the above *in situ* characterization results, the Cr-mediated dynamic reconstruction mechanism could be described as follows (Fig. 4c): CoO in the pristine electrocatalyst first captures electrons and is reduced to Co (eqn (1)); then, a spontaneous redox reaction occurs between Co and NO<sub>3</sub><sup>−</sup>, leading to the formation of Co(OH)<sub>2</sub> and NO<sub>2</sub><sup>−</sup> (eqn (2));<sup>26</sup> the formed Co(OH)<sub>2</sub> is then partially reduced to Co under the negative applied potentials (eqn (3)), finally achieving a dynamic balance between Co(OH)<sub>2</sub> and Co.



DFT calculations were further conducted to confirm the proposed dynamic reconstruction mechanism. The reconstruction energy of Cr-Co(OH)<sub>2</sub> was much lower than that of Co(OH)<sub>2</sub> (Fig. S43, ESI†), indicating that the conversion of Co(OH)<sub>2</sub> back to Co was more favorable with Cr modulation. To reveal the crucial role of the Cr dopant in tuning the reconstruction process, Bader charge analysis was conducted, which could help uncover the electronic structural changes of

Co after Cr doping. It was found that the charge transfer from the Co atom to the neighboring O atom was reduced, indicating weakened Co–OH interactions after Cr doping (Fig. S44, ESI†). Moreover, the projected density of states (PDOS) were utilized to analyze the orbital interaction between Co and –OH (Fig. S45, ESI†). It was found that with Cr doping, the electron states of the Co 3d and O 2p orbitals were upshifted toward the Fermi level, suggesting a weakened binding force between the Co atom and the O atom of the –OH group.<sup>27</sup> Therefore, the Cr dopant could weaken the electronic interaction between the Co atom and the –OH group, contributing to the conversion of Co(OH)<sub>2</sub> back to Co, thus achieving the dynamic reconstruction of Co(OH)<sub>2</sub> and Co.

### Reaction mechanism analysis

In addition to the detection of the reconstruction process, the *in situ* electrochemical Raman spectra could also be utilized to determine the reaction intermediates. For the Cr-doped electrocatalyst, the Raman signals at 1049 and 1525 cm<sup>−1</sup> were ascribed to the symmetric stretching mode of \*NO<sub>3</sub> and the N=O stretching vibration of \*NOH, respectively (Fig. 4b).<sup>28</sup> The peak intensity of the \*NOH intermediate gradually decreased with the negative shift of the potential, corresponding to the accelerated NO<sub>3</sub><sup>−</sup>RR kinetics with rapid intermediate consumption. Besides, the broad peak at 3398 cm<sup>−1</sup> could be ascribed to the O–H stretching of H<sub>2</sub>O, indicating the involvement of interfacial water in the electrocatalytic NO<sub>3</sub><sup>−</sup>RR process. The NO<sub>3</sub><sup>−</sup>RR reaction mechanism was further explored by *in situ* attenuated total reflection Fourier transform infrared spectroscopy (ATR-FTIR). As shown in the *in situ* ATR-FTIR spectra of the Cr-doped electrocatalyst (Fig. 5a), the upward bands appearing at 1245 and 1344 cm<sup>−1</sup> could be attributed to the asymmetric stretching vibrations of \*NO<sub>2</sub> and \*NO<sub>3</sub>.<sup>29</sup> The decreased intensity of the \*NO<sub>3</sub> peak with the negative shift of potential indicated an increased \*NO<sub>3</sub> consumption. The characteristic

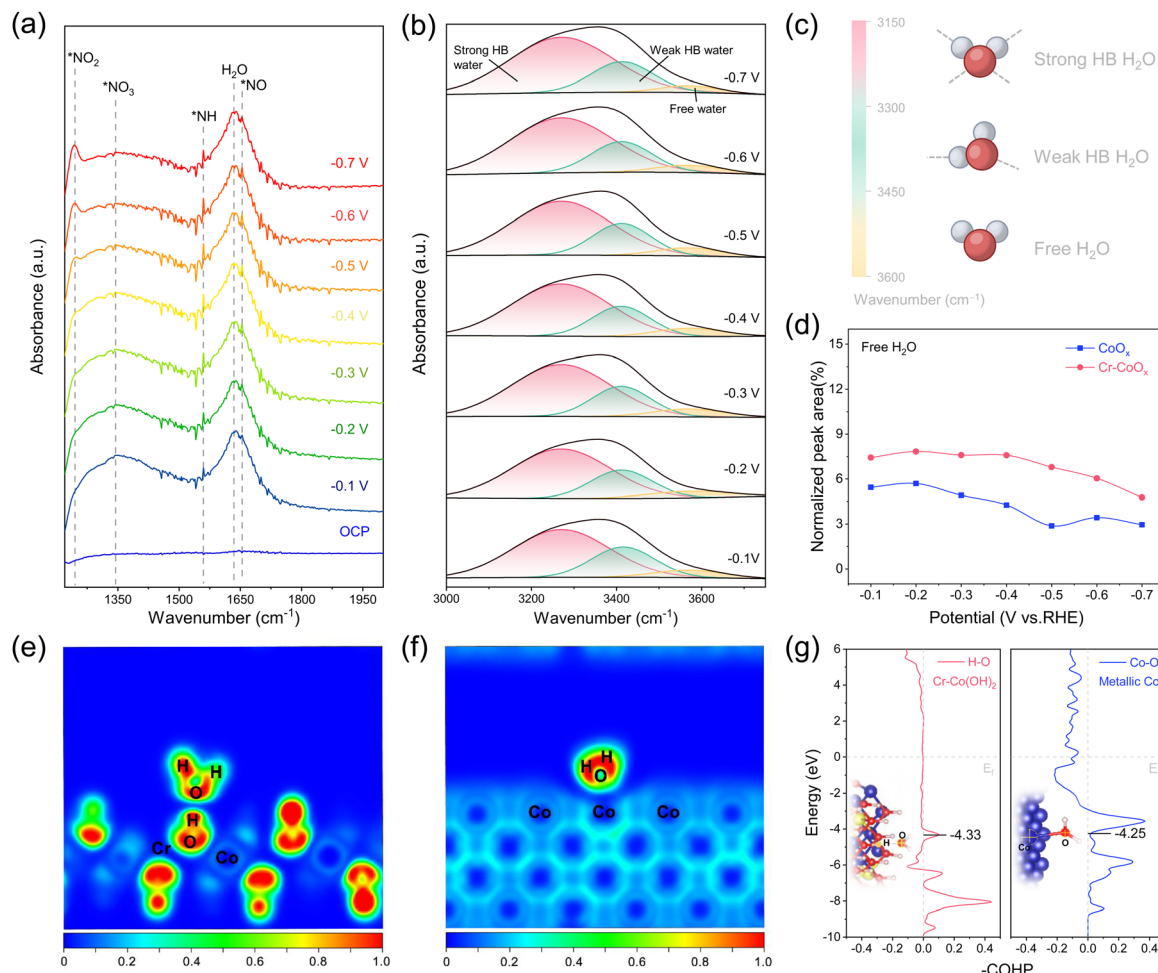


**Fig. 5** Intermediates and interfacial H<sub>2</sub>O structural analysis. (a) *In situ* ATR-FTIR spectra of the Cr-CoO<sub>x</sub> electrocatalyst at different applied potentials. (b) Potential-dependent *in situ* ATR-FTIR spectra of the O-H stretching mode of interfacial water on the Cr-CoO<sub>x</sub> electrocatalyst surface. (c) Schematic of H<sub>2</sub>O molecules with different hydrogen-bond structures. (d) Comparison of the free H<sub>2</sub>O relative content for the Cr-CoO<sub>x</sub> and CoO<sub>x</sub>. ELF evaluations for H<sub>2</sub>O adsorption on the (e) OH site of Cr-Co(OH)<sub>2</sub> and (f) the Co site of metallic Co. (g) pCOHP between the O atom of the adsorbed H<sub>2</sub>O and H atom of the OH site on Cr-Co(OH)<sub>2</sub> or the Co atom on the metallic Co. The insets show the structures of interfacial H<sub>2</sub>O adsorbed on different surfaces.

peaks located at 1559 and 1654 cm<sup>-1</sup> were ascribed to the N-H stretching vibration of \*NH and the N-O stretching vibration of \*NO.<sup>30</sup> Moreover, the H-O-H bending vibration of H<sub>2</sub>O was observed at 1634 cm<sup>-1</sup>. However, the CoO<sub>x</sub> electrocatalyst without Cr doping showed weak signals from the intermediates and H<sub>2</sub>O in the *in situ* ATR-FTIR spectra (Fig. S46, ESI†), corresponding to the weak interaction with interfacial H<sub>2</sub>O and slow NO<sub>3</sub><sup>-</sup>RR kinetics. Combining the *in situ* Raman and *in situ* ATR-FTIR results, the NO<sub>3</sub><sup>-</sup>RR reaction pathway of the Cr-doped electrocatalyst could be described as follows: \*NO<sub>3</sub> → \*NO<sub>2</sub> → \*NO → \*NOH → \*NH → \*NH<sub>2</sub> → \*NH<sub>3</sub>, which was consistent with the DFT results.

The interfacial water structure on the Cr-CoO<sub>x</sub> electrocatalyst surface was further investigated by *in situ* ATR-FTIR measurements (Fig. 5b). The broad O-H stretching peak of interfacial water located at 3000–3750 cm<sup>-1</sup> could be fitted into three distinct peaks, corresponding to the strong hydrogen-bonded (HB) H<sub>2</sub>O, weak HB H<sub>2</sub>O, and free H<sub>2</sub>O (Fig. 5c), respectively.<sup>31</sup> Compared with the other two types of interfacial

H<sub>2</sub>O, the free H<sub>2</sub>O had the lowest dissociation energy and the highest reactivity for participating in the hydrogenation process.<sup>32</sup> The Cr-doped electrocatalyst showed an increased content of free H<sub>2</sub>O compared with the electrocatalyst without Cr doping (Fig. 5d and Fig. S47, ESI†), indicating that the introduction of Cr could effectively modulate the interfacial water structure and increase the relative content of the highly reactive free H<sub>2</sub>O. Theoretical calculations were further performed to confirm the modulation mechanism of the interfacial hydrogen bonds by the Cr dopant. Electron localization function (ELF) evaluations showed that abundant valence electrons were distributed on the -OH sites of the Cr-Co(OH)<sub>2</sub> (Fig. 5e). This strong electron localization revealed the enhancement of the hydrogen-bonding interaction between the -OH group and the interfacial H<sub>2</sub>O molecule.<sup>33</sup> In comparison, Co exhibited a typical metallic-bonding nature with electron delocalization, showing weak interactions with the interfacial H<sub>2</sub>O molecule (Fig. 5f). Moreover, the projected crystal orbital Hamilton population (pCOHP) results showed that Cr-Co(OH)<sub>2</sub>



displayed a more reduced integrated COHP value ( $-4.33$  eV) than that of the metallic Co ( $-4.25$  eV) (Fig. 5g). The decreased antibonding state occupancy of Cr-Co(OH)<sub>2</sub> further revealed the strong bonding interaction between the O atom of the adsorbed H<sub>2</sub>O and the H atom of the OH site on the Cr-Co(OH)<sub>2</sub>.<sup>27</sup> Based on the *in situ* characterizations and theoretical calculations described above, it could be concluded that the -OH group of Cr-Co(OH)<sub>2</sub> strongly interacted with the interfacial H<sub>2</sub>O, dragging more free H<sub>2</sub>O from the strongly hydrogen-bonded bulk H<sub>2</sub>O for greater participation in the hydrogenation process in the NO<sub>3</sub><sup>-</sup>RR.

To identify the contribution of the Cr dopant to the boosted H<sub>2</sub>O dissociation, kinetic isotopic effect (KIE) tests were performed with the substitution of D<sub>2</sub>O for H<sub>2</sub>O, in which the KIE value could be defined as the current density ratio measured in H<sub>2</sub>O and D<sub>2</sub>O.<sup>34</sup> At  $-0.4$  V vs. RHE, the Cr-doped electrocatalyst displayed the lowest KIE value of 1.26 (Fig. S48, ESI†), revealing that doping with Cr could promote the H<sub>2</sub>O-dissociation process and improve the active hydrogen (\*H) supply. When adding tertiary butanol (TBA) to quench \*H, the current density and NH<sub>3</sub> yield rate were greatly reduced (Fig. S49, ESI†), indicating the significant role of \*H in the hydrogenation process of the NO<sub>3</sub><sup>-</sup>RR.<sup>35</sup> Next, Bode phase plots showed that Cr doping could induce a shift of the phase angle peak toward higher frequency and lower intensity (Fig. S50, ESI†), revealing the accelerated H<sub>2</sub>O dissociation and improved NO<sub>3</sub><sup>-</sup>RR reaction kinetics.<sup>36</sup>

## Conclusions

In summary, a Cr-doping strategy was proposed to modulate the reconstruction process and tune the interfacial hydrogen-bonding interactions of the Co-based catalysts. MD simulations combined with DFT calculations revealed that the Cr-doped Co(OH)<sub>2</sub> could disturb the rigid hydrogen-bond network and facilitate interfacial H<sub>2</sub>O dissociation, thereby providing \*H and boosting the hydrogenation conversion of NO<sub>3</sub><sup>-</sup> into NH<sub>3</sub> on the metallic Co site. As a proof of concept, the Cr-doped Co-based materials were prepared by an ion exchange and subsequent calcination process. The as-prepared Cr-doped electrocatalyst achieved excellent catalytic NO<sub>3</sub><sup>-</sup>RR activity with a high NH<sub>3</sub> faradaic efficiency of 97.36% and a high NH<sub>3</sub> yield rate of 58.92 mg h<sup>-1</sup> cm<sup>-2</sup>. *In situ* XRD, *in situ* Raman, and DFT calculations showed that Cr doping could modulate the reconstruction process, achieving a dynamic balance of Co(OH)<sub>2</sub> and Co. *In situ* ATR-FTIR and DFT calculations further indicated that the Cr-doping in Co(OH)<sub>2</sub> could drag more free H<sub>2</sub>O from the rigid water network to participate in the hydrogenation process in the NO<sub>3</sub><sup>-</sup>RR. This work provides guidance for elaborately designing dynamic catalysts with tunable interfacial hydrogen-bonding interactions to boost electrocatalytic ammonia synthesis.

## Author contributions

Y. Wan conceived the project and wrote the manuscript. Y. Tang, K. Sun, Z. Zhuang, and Y. Zheng conducted the material

synthesis, physical characterization, and electrochemical tests. Y. Zuo performed the theoretical calculations. W. Yan, J. Zhang, and R. Lv supervised the project.

## Data availability

The data supporting the findings of this study are available in the ESI† of this article.

## Conflicts of interest

There are no conflicts to declare.

## Acknowledgements

This work was supported by the National Natural Science Foundation of China (52402045, 52371228), the Natural Science Foundation of Fujian Province (2024J01256), and the Pilot Group Program of the Research Fund for International Senior Scientists (22250710676). We thank Shenzhen HUASUAN technology Co., Ltd for assistance with the theoretical calculations. We thank Shiyanjia Lab ([www.shiyanjia.com](http://www.shiyanjia.com)) for the XPS and TEM tests.

## Notes and references

- 1 X. Fu, J. B. Pedersen, Y. Zhou, M. Saccoccio, S. Li, R. Sažinas, K. Li, S. Z. Andersen, A. Xu, N. H. Deissler, J. B. V. Mygind, C. Wei, J. Kibsgaard, P. C. K. Vesborg, J. K. Nørskov and I. Chorkendorff, *Science*, 2023, **379**, 707–712.
- 2 Q. Gao, B. Yao, H. S. Pillai, W. Zang, X. Han, Y. Liu, S.-W. Yu, Z. Yan, B. Min, S. Zhang, H. Zhou, L. Ma, H. Xin, Q. He and H. Zhu, *Nat. Synth.*, 2023, **2**, 624–634.
- 3 B. H. R. Suryanto, K. Matuszek, J. Choi, R. Y. Hodgetts, H.-L. Du, J. M. Bakker, C. S. M. Kang, P. V. Cherepanov, A. N. Simonov and D. R. MacFarlane, *Science*, 2021, **372**, 1187–1191.
- 4 Y. Wan, M. Zheng, W. Yan, J. Zhang and R. Lv, *Adv. Energy Mater.*, 2024, **14**, 2303588.
- 5 K. Wang, R. Mao, R. Liu, J. Zhang, H. Zhao, W. Ran and X. Zhao, *Nat. Water*, 2023, **1**, 1068–1078.
- 6 X. Fu, *Chin. J. Catal.*, 2023, **53**, 8–12.
- 7 Y. Wei, J. Huang, H. Chen, S.-J. Zheng, R.-W. Huang, X.-Y. Dong, L.-K. Li, A. Cao, J. Cai and S.-Q. Zang, *Adv. Mater.*, 2024, **36**, 2404774.
- 8 C. Zhang, Y. Zhang, R. Deng, L. Yuan, Y. Zou, T. Bao, X. Zhang, G. Wei, C. Yu and C. Liu, *Adv. Mater.*, 2024, **36**, 2313844.
- 9 Z. Chang, G. Meng, Y. Chen, C. Chen, S. Han, P. Wu, L. Zhu, H. Tian, F. Kong, M. Wang, X. Cui and J. Shi, *Adv. Mater.*, 2023, **35**, 2304508.
- 10 W. Zhu, F. Yao, Q. Wu, Q. Jiang, J. Wang, Z. Wang and H. Liang, *Energy Environ. Sci.*, 2023, **16**, 2483–2493.

- 11 S. Ye, Z. Chen, G. Zhang, W. Chen, C. Peng, X. Yang, L. Zheng, Y. Li, X. Ren, H. Cao, D. Xue, J. Qiu, Q. Zhang and J. Liu, *Energy Environ. Sci.*, 2022, **15**, 760–770.
- 12 K. Yang, S.-H. Han, C. Cheng, C. Guo, T. Li and Y. Yu, *J. Am. Chem. Soc.*, 2024, **146**, 12976–12983.
- 13 S. Han, H. Li, T. Li, F. Chen, R. Yang, Y. Yu and B. Zhang, *Nat. Catal.*, 2023, **6**, 402–414.
- 14 L. Qiao, A. Zhu, D. Liu, K. An, J. Feng, C. Liu, K. W. Ng and H. Pan, *Adv. Energy Mater.*, 2024, 2402805, DOI: [10.1002/aenm.202402805](https://doi.org/10.1002/aenm.202402805).
- 15 B. Zhou, L. Yu, W. Zhang, X. Liu, H. Zhang, J. Cheng, Z. Chen, H. Zhang, M. Li, Y. Shi, F. Jia, Y. Huang, L. Zhang and Z. Ai, *Angew. Chem., Int. Ed.*, 2024, **63**, e202406046.
- 16 Y.-H. Wang, S. Zheng, W.-M. Yang, R.-Y. Zhou, Q.-F. He, P. Radjenovic, J.-C. Dong, S. Li, J. Zheng, Z.-L. Yang, G. Attard, F. Pan, Z.-Q. Tian and J.-F. Li, *Nature*, 2021, **600**, 81–85.
- 17 X. H. Chen, X. L. Li, T. Li, J. H. Jia, J. L. Lei, N. B. Li and H. Q. Luo, *Energy Environ. Sci.*, 2024, **17**, 5091–5101.
- 18 W. Liu, M. Xia, C. Zhao, B. Chong, J. Chen, H. Li, H. Ou and G. Yang, *Nat. Commun.*, 2024, **15**, 3524.
- 19 K. Fan, W. Xie, J. Li, Y. Sun, P. Xu, Y. Tang, Z. Li and M. Shao, *Nat. Commun.*, 2022, **13**, 7958.
- 20 Y. Xu, C. Cheng, J. Zhu, B. Zhang, Y. Wang and Y. Yu, *Angew. Chem., Int. Ed.*, 2024, **63**, e202400289.
- 21 P. Li, Y. Jiang, Y. Hu, Y. Men, Y. Liu, W. Cai and S. Chen, *Nat. Catal.*, 2022, **5**, 900–911.
- 22 X. Wang, X. Liu, J. Fang, H. Wang, X. Liu, H. Wang, C. Chen, Y. Wang, X. Zhang, W. Zhu and Z. Zhuang, *Nat. Commun.*, 2024, **15**, 1137.
- 23 S. Xu, D. Jiao, X. Ruan, Z. Jin, Y. Qiu, Z. Feng, L. Zheng, J. Fan, W. Zheng and X. Cui, *Adv. Funct. Mater.*, 2024, **34**, 2401265.
- 24 X. Chen, Y. Cheng, B. Zhang, J. Zhou and S. He, *Nat. Commun.*, 2024, **15**, 6278.
- 25 H. Ze, Z.-L. Yang, M.-L. Li, X.-G. Zhang, Y.-L. A, Q.-N. Zheng, Y.-H. Wang, J.-H. Tian, Y.-J. Zhang and J.-F. Li, *J. Am. Chem. Soc.*, 2024, **146**, 12538–12546.
- 26 S. Liang, X. Teng, H. Xu, L. Chen and J. Shi, *Angew. Chem., Int. Ed.*, 2024, **63**, e202400206.
- 27 Q. Wen, J. Duan, W. Wang, D. Huang, Y. Liu, Y. Shi, J. Fang, A. Nie, H. Li and T. Zhai, *Angew. Chem., Int. Ed.*, 2022, **61**, e202206077.
- 28 J.-Y. Fang, Q.-Z. Zheng, Y.-Y. Lou, K.-M. Zhao, S.-N. Hu, G. Li, O. Akdim, X.-Y. Huang and S.-G. Sun, *Nat. Commun.*, 2022, **13**, 7899.
- 29 L. Yang, C. Wang, Y. Li, W. Ge, L. Tang, J. Shen, Y. Zhu and C. Li, *Adv. Funct. Mater.*, 2024, **34**, 2401094.
- 30 Y. Huang, C. He, C. Cheng, S. Han, M. He, Y. Wang, N. Meng, B. Zhang, Q. Lu and Y. Yu, *Nat. Commun.*, 2023, **14**, 7368.
- 31 K. Sun, X. Wu, Z. Zhuang, L. Liu, J. Fang, L. Zeng, J. Ma, S. Liu, J. Li, R. Dai, X. Tan, K. Yu, D. Liu, W.-C. Cheong, A. Huang, Y. Liu, Y. Pan, H. Xiao and C. Chen, *Nat. Commun.*, 2022, **13**, 6260.
- 32 L.-f Shen, B.-a Lu, Y.-y Li, J. Liu, Z.-c Huang-fu, H. Peng, J.-y Ye, X.-m Qu, J.-m Zhang, G. Li, W.-b Cai, Y.-x Jiang and S.-g Sun, *Angew. Chem., Int. Ed.*, 2020, **59**, 22397–22402.
- 33 S. Zhu, R. Yang, H. J. W. Li, S. Huang, H. Wang, Y. Liu, H. Li and T. Zhai, *Angew. Chem., Int. Ed.*, 2024, **63**, e202319462.
- 34 Q. Hu, K. Yang, O. Peng, M. Li, L. Ma, S. Huang, Y. Du, Z.-X. Xu, Q. Wang, Z. Chen, M. Yang and K. P. Loh, *J. Am. Chem. Soc.*, 2024, **146**, 668–676.
- 35 Y. Li, C. Wang, L. Yang, W. Ge, J. Shen, Y. Zhu and C. Li, *Adv. Energy Mater.*, 2024, **14**, 2303863.
- 36 J. Guan, L. Cai, W. Li, H. Zhou and Y. Huang, *Appl. Catal., B*, 2024, **358**, 124387.